Effect of blockage on wind turbine power and wake development

Olivier Ndindayino , Augustin Puel , and Johan Meyers

Department of Mechanical Engineering, KU Leuven, Celestijnenlaan 300, B3001 Leuven, Belgium

Correspondence: Olivier Ndindayino (olivier.ndindayino@kuleuven.be)

Abstract. Recent work by Lanzilao & Meyers (J. Fluid Mech, 2024) has shown that wind-farm blockage introduces an unfavourable pressure gradient in front of the farm and a favourable pressure gradient in the farm, which are strongly correlated with the nonlocal efficiency and wake efficiency respectively. In particular, the favourable pressure gradient in the farm increases the farm wake efficiency, defined as the average farm power normalized by the average front-row power. Here, we investigate the impact of blockage on wake development and power of wind turbines using an idealized large-eddy simulation setup in which blockage conditions are artificially introduced using a rigid-lid, further also using neutral stratification and no wind veer. We simulate both infinite and finite single turbine rows, as well as a setup with two staggered rows. Blockage strength is adjusted by varying the boundary layer height (H) and turbine spacing (S). We find that blockage strongly affects near wake behaviour, altering Froude momentum theory, by introducing a favourable pressure difference (Δp_{NW}) across the turbine row. The same setup also leads to an unfavourable pressure difference (Δp_{FW}) in the far wake, which simply follows from the rigid-lid conditions and the change of momentum flux due to wake recovery. A strong positive correlation was observed of $-\Delta p_{NW}$ with both power coefficient (C_P) and thrust coefficient (C_T). Specifically, as S and H decrease, $-\Delta p_{NW}$, C_P and C_T increase. At the same time a lower induction is observed at the rotor disk, and a lower wake deficit in the near wake. The reduction of near wake velocity deficit as a result of blockage also translates into lower deficits and wake widths in the far wake. When scaling the far wake development with initial far wake deficit and width, we do not see a direct effect of the adverse pressure gradient on the wake recovery. However, we do see a profound effect of H on the wake recovery, with higher boundary layers leading to faster recovery. This relates to the fact that, the wake can more freely expand vertically in high-boundary layer cases, into a larger region of high-speed flow than for shallow boundary layers. Finally, we introduce a simplified Froude momentum balance to parametrize the relation between blockage, pressure drop and near wake properties, and compare it to the LES results.

1 Introduction

In large wind farms, significant flow slowdown occurs upstream of the farm, called blockage. Measurements conducted by (Bleeg et al., 2018) before and after wind farm commissioning revealed significant reductions of wind speed upstream of the farm (up to 4% for 10 rotor diameters). Around the same time Allaerts and Meyers (2017, 2018) described the excitation of gravity waves in their wind-farm large-eddy simulations, also observing significant slow down of wind speed in front of the farm. Since then, various other studies have also discussed the excitation of gravity waves by wind farms, and related blockage
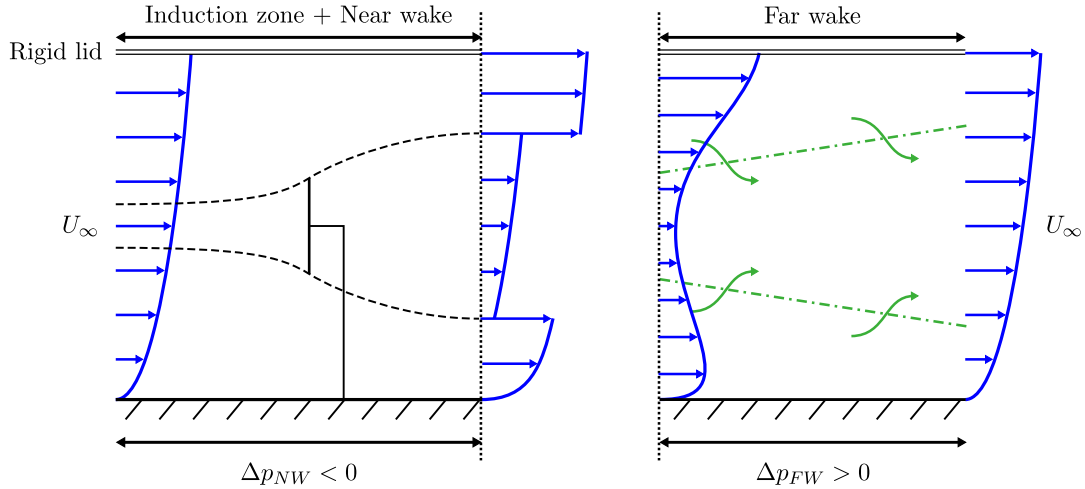
Figure 1. Sketch (side view) of a single turbine row (infinitely wide) inside an idealised ABL with rigid-lid top condition.

effects (Wu and Porté-Agel, 2017; Maas, 2023; Stipa et al., 2024). Recently, Lanzilao and Meyers (2024) performed LES simulations of a fixed 1.6 GW wind farm in different atmospheric stratified conditions to investigate effects on wind-farm efficiency, blockage and related gravity-wave excitation. They found that the upstream slowdown associated with blockage is

30 dominantly originating from the vertical displacement of the capping inversion at the top the boundary layer, and the associated hydrostatic pressure induced by the increased column of cold (higher density) air below the inversion. For the atmosphere conditions considered in their simulations, purely hydrodynamic blockage effects (i.e. associated with Bernoulli's law and induction by the turbines, see also Segalini and Dahlberg, 2020) were at least an order of magnitude smaller (Lanzilao and Meyers, 2022, 2024).

35   Similar to Allaerts and Meyers (2017, 2018), Lanzilao and Meyers (2024) identified a strong unfavourable pressure gradient upstream of the farm, but also a favourable pressure gradient within the wind farm. Defining the non-local efficiency $\eta_{nl} = P_1/P_\infty$ as the ratio between the power of a free standing turbine P_∞ and the average turbine power of the first row of a wind farm P_1, and a wake efficiency $\eta_w = P_{tot}/(N_t P_1)$ as the ratio between the average turbine power in the wind farm (P_{tot}/N_t) and the average turbine power of the first row, they found a strong negative correlation between the unfavourable upstream

40 pressure gradient and η_{nl}, and a strong positive correlation between the favourable pressure gradient within the farm and η_w. It was further found that, depending on atmospheric conditions, the beneficial effects of the favourable pressure gradient can offset the negative effects of the upstream unfavourable pressure gradient, sometimes leading a larger farm efficiency than in a similar fully neutral case without free-atmosphere stratification.

     In the current manuscript, our aim is to better understand the relationship between favourable pressure gradient and improved

45 efficiency using a new set of large-eddy simulations. To this end, we strongly simplify the simulation setup by replacing blockage induced by free-atmosphere stratification with blockage induced by a rigid-lid at the top of the boundary layer. Such a rigid-lid condition could be the equivalent of an infinitely strong capping inversion. Although such a condition cannot

exist, since the strongest density jump conceivable over the capping inversion should be well below the difference between density at 1 atm and vacuum, rigid-lid blockage nonetheless shows some similarities with blockage induced by free-atmosphere stratification (Smith, 2024). The advantage of using a rigid-lid condition is that the relationship between blockage, pressure gradient and efficiency is easier to quantify. This is illustrated in Fig. 1, for a single infinitely wide row of turbines. Looking at a control volume around the near wake and induction region of a turbine, it is directly clear that a favourable pressure difference should exist ($\Delta p_{NW} < 0$) – presuming negligible friction at the ground, this is a direct result from Newton's second law, the presence of the turbine thrust force, and continuity (so that outflowing momentum is larger than inflowing momentum). Similarly, an unfavourable pressure difference ($\Delta p_{FW} > 0$) should exist in the far wake. Moreover, considering near wake and far wake together, we find

$$HS(\Delta p_{NW} + \Delta p_{FW} + \Delta p_{bg}) + F_T + F_{fric} = 0, \tag{1}$$

with H the boundary layer height, S the spanwise spacing between turbines in the infinite row, F_T (> 0) the turbine thrust, F_{fric} (> 0) is friction from the ground and Δp_{bg} (< 0) is the background pressure difference in the absence of the turbines. We assume that $F_{fric} \approx \Delta p_{bg}$, thus Δp_{NW} and Δp_{FW} are dynamic pressure perturbations, superimposed on the background pressure. From Eq. (1), we expect $|\Delta p_{NW}| \gg |\Delta p_{FW}|$, which allows us to hypothesize that the effect of blockage on efficiency may be mostly related to changes in the near-waking behaviour.

The effects of domain blockage by rigid boundaries on turbine performance have been studied before, mostly in the context of blockage corrections in wind tunnel experiments of single model wind turbines (Mikkelsen and Sørensen, 2002; Werle, 2010; Segalini and Inghels, 2014). In these studies, the focus was on estimating free-flow conditions, thus eliminating the effects of wind tunnel walls. These corrections, were built by extending Froude momentum theory (Froude, 1889) to account for the pressure gradients included by any (small) domain blockage present in the wind tunnel. Here, we will use similar ideas to develop a simple model that correlates favourable pressure gradients induced by blockage with near wake induction and turbine power extraction, but now to quantify the effect of blockage rather than to exclude it. A similar approach was already used by Garrett and Cummins (2007) for tidal turbines in constant water level channels, and some elements were also used by Nishino and Willden (2012, 2013) for modelling the blockage effect of a finite array of tidal turbines in a wide channel cross section.

The setup of a row of closely spaced turbines that we are studying in the current work has also been explored in the past by McTavish et al. (2013, 2015); Strickland and Stevens (2020, 2022). They reported so called 'in-field' blockage, leading to increased power production of the turbines, which they attributed to mutual favourable interactions between turbines. However, by performing a careful domain sensitivity study, Bleeg and Montavon (2022) later showed that these beneficial effects disappear when the domain size is sufficiently large. Thus, in these earlier reports, power increase due to 'in-field' blockage was effectively a result of domain blockage, and consequently may be related to the increased wake efficiency observed by Lanzilao and Meyers (2024) under favourable pressure gradient conditions.

Looking at the sketch in Fig. 1 and referring to the discussion above, an unfavourable pressure gradient is expected in the far wake, albeit much smaller than the favourable pressure gradient in the near wake. The effects of pressure gradients on wake

development have been studied by Liu et al. (2002); Shamsoddin and Porté-Agel (2017) for plane wakes, and by Shamsoddin and Porté-Agel (2018) for axisymmetric wakes, and later more general conditions were also considered by Dar and Porté-Agel (2022). All of these studies conclude that unfavourable pressure gradients lead to slower, and favourable pressure gradients

85   to faster wake recovery. However, we note already that for all simulations considered in the current manuscript, we found the unfavourable pressure gradients in the far wake to be much smaller than the values appearing in above studies, so that wake recovery is unaffected by them.

In the current work, we setup a range of large-eddy simulations of a neutral rigid-lid pressure driven boundary layer, in which we represent both infinite and finite single turbine rows, as well as a setup with staggered rows. Blockage strength is

90   adjusted by varying the boundary layer height (H) and turbine spacing (S). Simulation results are further compared to a simple model that extends classical Froude momentum theory, parametrizing the effects of pressure gradients on wind turbine power, thrust, and induction. Such a model can straightforwardly be incorporated into engineering blockage and wake models such as, e.g., WAYVE Allaerts and Meyers, 2019; Devesse et al., 2022; Stipa et al., 2024; Devesse et al., 2024a, b, in which large-scale pressure gradients coming from free-atmosphere stratification and gravity wave feedback are available. The latter is however a

95   topic of future research and not in the scope of the current manuscript.

The article is structured as follows. The setup of the LES simulations are elaborated in Sect. 2. The extension of the Froude momentum theory is discussed in Sect. 3. Next, Sect. 4 presents the LES results, for the far and near wake analysis, including model validation. Lastly, conclusions are provided in Sect. 5.

2   Methodology

2.1   Governing equations

We consider the filtered Navier–Stokes equations for a neutral pressure-driven boundary layer, given by

$$\frac{\partial \tilde{u}_i}{\partial x_i} = 0, \tag{2}$$

$$\frac{\partial \tilde{u}_i}{\partial t} + \tilde{u}_j \frac{\partial \tilde{u}_i}{\partial x_j} = -\frac{1}{\rho}\frac{\partial \tilde{p}^*}{\partial x_i} - \frac{1}{\rho}\frac{\mathrm{d}p_\infty}{\mathrm{d}x_1}\delta_{1i} - \frac{\partial \tau_{ij}^{sgs}}{\partial x_j} + f_i, \tag{3}$$

where, the horizontal and vertical directions are represented by indices $i = 1, 2$ and 3, with $(x_1, x_2, x_3) = (x, y, z)$. The filtered

105   velocity components are denoted by $\tilde{u}_i$ for the three-dimensional flow field, with $(\tilde{u}_1, \tilde{u}_2, \tilde{u}_3) = (\tilde{u}, \tilde{v}, \tilde{w})$. The filtered modified pressure is defined as $\tilde{p}^* = \tilde{p} - p_\infty + \rho_0 \tau_{kk}/3$, where p_∞ represents the mean background pressure, and $\tau_{kk}/3$ denotes the trace of the subgrid-scale stress tensor $\tau_{ij} = \widetilde{u_i u_j} - \tilde{u}_i \tilde{u}_j$, and where a subgrid-scale model is used to model the anisotropic component of the residual-stress tensor $\tau_{ij}^{sgs} = \tau_{ij} - \delta_{ij}\tau_{kk}/3$. The forces (per unit of density) f_i exerted by the wind turbines on the flow are modelled using a non-rotating actuator disk model (Goit and Meyers, 2015) with a Shapiro correction factor

110   (Shapiro et al., 2019) to avoid over prediction of turbine power on typical LES grid resolutions.

The governing equations (2–3) are solved using the SP-Wind solver, an in-house software developed at KU Leuven (Calaf et al., 2010; Goit and Meyers, 2015; Munters et al., 2016; Allaerts and Meyers, 2017; Lanzilao and Meyers, 2024). The
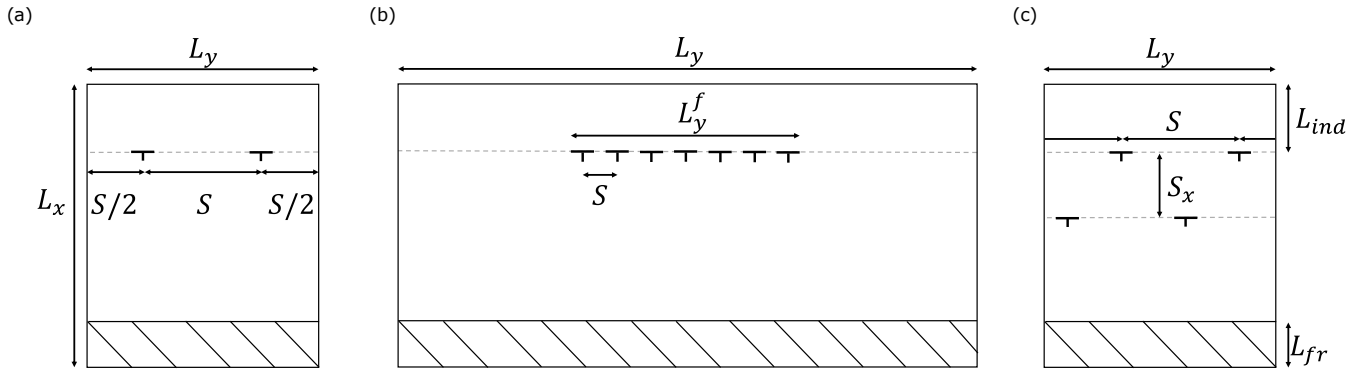
Figure 2. The plane view of (a) infinite row, (b) finite row and (c) infinite staggered rows computational main domain.

equations are integrated over time using a standard fourth-order Runge–Kutta scheme, with the time step determined by a Courant–Friedrichs–Lewy (CFL) number of 0.4. Discretization in horizontal directions is performed using a Fourier pseudo-spectral method, employing the 3/2 dealising rule. In the vertical direction, an energy-preserving fourth-order finite difference scheme is applied (Verstappen and Veldman, 2003). Continuity is enforced by a direct solve of the Poisson equation at each stage of the Runge–Kutta method. The influence of subgrid-scale motions on the resolved flow is captured by the Smagorinsky model in combination with Mason and Thomson (1992) wall damping, using a Smagorinsky length $\ell_s^{-n} = (C_s\Delta)^{-n} + [\kappa(z + z_0)]^{-n}$, with $C_s = 0.14$, and $n = 1$, Δ the grid spacing, and $\kappa = 0.41$ the Von Karman constant. This is consistent with prior studies using SP-Wind (Meyers, 2011; Allaerts and Meyers, 2017; Lanzilao and Meyers, 2024). We also refer to Calaf et al. (2010); Lignarolo et al. (2016); Martínez-Tossas et al. (2018); Sood et al. (2022) for code benchmarking, and validation.

2.2 Simulation setup

Figure 2 provides an overview of the different simulations setups considered in the current study, and a list of all cases is provided in Table 1. All turbines correspond to the International Energy Agency (IEA) 15 MW offshore reference wind turbine (Gaertner et al., 2020), with hub height $z_h = 150$ m and diameter $D = 240$ m. Conditions are such that the turbines operate bellow their rated power. Consequently, a constant disk-based thrust coefficient is $C_t' = 1.44$ (Calaf et al., 2010), is used as an input parameter for the simulations.

First of all, a set of single infinite-row simulations are considered (Fig. 2a). We select a domain width $L_y = 9.6$ km with spanwise periodic boundary conditions, and by varying the number of turbines in the domain, we can change the turbine spacing S. Secondly, we also consider a finite row setup consisting of 7 turbines (Fig. 2b). Here, we take $L_y = 50$ km, so that $L_y/L_y^f \approx 7$ for the case with widest spacing ($S = 5$), following Lanzilao and Meyers (2024) who recommend $L_y/L_y^f \geq 6$ to avoid artificial effects from spanwise boundaries. Finally (Fig. 2c), two infinitely wide staggered rows of turbines are also considered, with $S_x/D = 5$, also using a domain width of $L_y = 9.6$ km.

The simulation domain $L_x \times L_y \times H$ is further selected as follows. All simulations use $L_x = 20$km, with an upstream region $L_{ind} = 4$ km in front of the turbines, and a fringe region length $L_{fr} = 2.6$ km. Different boundary layer heights are considered,

Table 1. Overview of the wind farm simulation cases and their computational domain dimensions $L_x \times L_y \times H$, the turbine spacing S/D and row averaged power coefficient $\langle C_P \rangle_{row}$ and thrust coefficient $\langle C_T \rangle_{row}$ (values of both rows are shown for the infinite staggered row simulations).

Cases	$L_x \times L_y \times H$ (km³)	S/D	$\langle C_P \rangle_{row}$	$\langle C_T \rangle_{row}$
Inf-H350-S2.5	$20 \times 9.6 \times 0.35$	2.5	0.7036	0.8933
Inf-H350-S5	$20 \times 9.6 \times 0.35$	5	0.6361	0.8352
Inf-H350-S10	$20 \times 9.6 \times 0.35$	10	0.6067	0.8092
Inf-H350-S20	$20 \times 9.6 \times 0.35$	20	0.5912	0.7954
Inf-H350-S40	$20 \times 9.6 \times 0.35$	40	0.5825	0.7877
Inf-H500-S2.5	$20 \times 9.6 \times 0.50$	2.5	0.6689	0.8637
Inf-H500-S5	$20 \times 9.6 \times 0.50$	5	0.6208	0.8217
Inf-H500-S10	$20 \times 9.6 \times 0.50$	10	0.5999	0.8032
Inf-H500-S20	$20 \times 9.6 \times 0.50$	20	0.5880	0.7926
Inf-H500-S40	$20 \times 9.6 \times 0.50$	40	0.5807	0.7860
Inf-H700-S2.5	$20 \times 9.6 \times 0.70$	2.5	0.6434	0.8416
Inf-H700-S5	$20 \times 9.6 \times 0.70$	5	0.6047	0.8075
Inf-H700-S40	$20 \times 9.6 \times 0.70$	40	0.5791	0.7845
Fin-H500-S2.5	$20 \times 50 \times 0.50$	2.5	0.6113	0.8128
Fin-H500-S5	$20 \times 50 \times 0.50$	5	0.6029	0.8054
Inf-H500-S5-stag	$20 \times 9.6 \times 0.50$	5	0.6171; 0.6151	0.8180; 0.8163
Inf-H500-S10-stag	$20 \times 9.6 \times 0.50$	10	0.5921; 0.5944	0.7957; 0.7978

i.e. $H = 350$, 500 and 700 m. All simulations use a wall stress boundary conditions at the bottom (with a surface roughness $z_0 = 10^{-4}$ m, which is a typical offshore value (Taylor and Yelland, 2001)), and symmetry conditions at the top. Boundary conditions in the horizontal directions are periodic, as a result of our pseudo-spectral discretization method. To break the periodicity in the streamwise direction and prescribe an inflow condition, we use a fringe-region technique to drive the main

140   domain by turbulent fully developed statistically steady flow fields obtained from a concurrent precursor simulation (Stevens et al., 2014). To prevent persistent spanwise locking of large-scale streamwise turbulent structures, a shifted periodic boundary condition is applied within the fringe-region, bypassing the need of excessive streamwise domain lengths (Munters et al., 2016).

    The precursor simulation domain $L_x^p \times L_y^p \times H$ is defined as follows. Three different precursor simulations are performed

145   for the infinite row cases, i.e. $L_x^p = 10$ km and $L_y^p = 9.6$ with a height of $H = 350$, 500 and 700 m. One additional precursor simulation is performed for the finite row cases, with $L_x^p = L_y^p = 10$ km and $H = 500$ m. However, since the fringe region

spans the full width and height of the main domain, SP-Wind requires matching heights and widths between the precursor and main domain when they run concurrently. To achieve this, the tiling technique of Sanchez Gomez et al. (2023) is used to extend the precursor flow fields in the y direction from 10 to 50 km. All precursor simulations are driven by a constant pressure

150   gradient $\mathrm{d}p_\infty/\mathrm{d}x_1 = -u_\tau^2/H$, with a friction velocity $u_\tau \approx 0.275$ ms^{-1}. Finally, all simulations and domains use the same grid resolution, i.e. $\Delta x = 40$ m, $\Delta y = 24$ m and $\Delta z = 7.93$ m in the streamwise, spanwise and vertical directions, respectively. This is consistent with resolutions used earlier in e.g., (Allaerts and Meyers, 2017, 2018; Lanzilao and Meyers, 2024).

    Precursor simulations are initialized using a log profile $u = (u_\tau/\kappa)ln(z/z_0)$ in combination with random noise and simulated for 20000 seconds, such that a fully developed statistically stationary pressure-driven boundary layer can develop.

155   Subsequently, the precursor domain and main domain are run concurrently for another 3000 seconds for the main domain to fully develop given the precursor inflow. Finally, precursor and main domain are concurrently progressed for an averaging time T_{av} of 10000 seconds.

3   Froude momentum theory with blockage
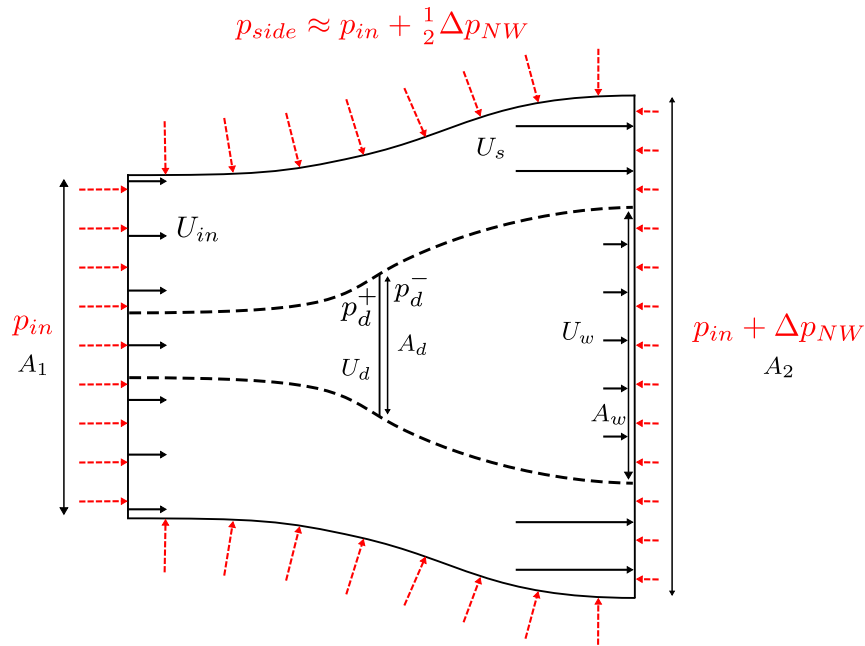
Figure 3. General setup of the control volume around a turbine to define blockage effects.

    We extend the Froude momentum theory to parametrize the relation between blockage, pressure drop and near wake proper-

160   ties for a single turbine present within a row or farm. The model is an extension of classic axial momentum theory developed by Rankine (1865) and Froude (1889). A similar approach was, e.g., used by Werle (2010) and Segalini and Inghels (2014) to derive blockage corrections for wind tunnels, or by Garrett and Cummins (2007) in the context of tidal turbines, although we

start from a slightly more general formulation that does not define inlet and outlet areas of the control volume in advance (see Fig. 3).

165   Consider a control volume around a single turbine within a row or farm (Fig. 3) that is based on a streamtube, extending from the the start of the induction zone until the end of the near wake. We choose the area $A_1 = SH$, which corresponds to the 'available' inflow for the turbine. Note that the outlet area A_2 is a priori unknown, but expected to be larger than A_1. In the case of an infinite row of turbines, $A_2 = A_1$ is obtained. We further define the disk area $A_d = \pi D^2/4$, and the wake area A_w, which is not known a priori.

170   We presume uniform inflow U_{in} into the control volume, and uniform pressures p_{in} and $p_{in} + \Delta p_{NW}$ over inlet and outlet, respectively. Furthermore, the disk velocity $U_d = U_{in}(1-a)$, with a the axial induction factor. This leads to a thrust force $F_T = 1/2\rho C'_T U_{in}^2 (1-a)^2 A_d$, and in absence of drag or mechanical losses, also to $P = 1/2\rho C'_T U_{in}^3 (1-a)^3 A_d$.

First, applying the principle of conservation of mass on the entire streamtube and for the streamtube that passes through the rotor, we obtain

175
$$A_d U_{in}(1-a) = A_w U_w, \tag{4}$$

$$A_w U_w + (A_2 - A_w)U_s = A_1 U_{in}. \tag{5}$$

Secondly, we apply the principle of conservation of momentum in the streamwise direction over the entire streamtube. Similar to Eq. (1), we presume that the friction at the ground is balanced by the background pressure difference present in the absence of a turbine ($F_{fric} \approx \Delta p_{bg}$), so that, to first order, Δp_{NW} contains the pressure perturbations due to the presence of the wind

180   turbines only. A similar strategy was, e.g., used by Kirby et al. (2023). As a result, the momentum balance equation is,er the entire steamtube results in]

$$-\frac{1}{2}C'_T U_{in}^2(1-a)^2 A_d - \frac{1}{2\rho}\Delta p_{NW}(A_1 + A_2) = (A_2 - A_w)U_s^2 + A_w U_w^2 - A_1 U_{in}^2, \tag{6}$$

where the density ρ is a known constant value. Here, we have further presumed that the average pressure on the mantle of the streamtube, corresponds approximately to $p_{side} \approx p_{in} + \Delta p_{NW}/2$. Thirdly, using $F_T = (p^+ - p^-)A_d$, and eliminating p^+

185   and p^- using Bernoulli for streamlines in front and behind the disk respectively (similar to what is done in derivations of the classical Betz theory), we arrive at

$$\frac{1}{2}C'_T U_{in}^2(1-a)^2 = \frac{1}{2}U_{in}^2 - \frac{1}{2}U_w^2 - \frac{1}{\rho}\Delta p_{NW}. \tag{7}$$

Finally, using Bernoulli for streamlines that do not pass through the rotor area, we also find

$$\frac{1}{2}U_{in}^2 = \frac{1}{\rho}\Delta p_{NW} + \frac{1}{2}U_s^2 \tag{8}$$

190   Above leads to a set of five model equations: (Eqs. 4–8), with in principle four known input variables A_1, A_d, C'_t and U_{in}, which leaves six unknown variables: a, U_w, U_s, A_w, A_2, and Δp_{NW}. Thus we lack one equation to arrive at a closed system.

There are two situations that lead to a simple closure of the system. First of all, imposing $\Delta p_{NW} = 0$ leads to the classical Betz–Joukowsky theory for a single isolated turbine. The other case corresponds to a infinite row of turbines, in which case

$A_2 = A_1 = SH$. This leads to the wind tunnel blockage corrections earlier discussed (e.g., Werle, 2010 and Segalini and Inghels, 2014; note that a converging or diverging wind tunnel would require a known $A_2 \neq A_1$).

In the more general setting of a finite row of turbines, neither A_2 nor Δp_{NW} are known a priori. At the sides of a finite row, turbines have clearly more space to expand sideways, and possibly a lower Δp_{NW} applies than in the centre of the row, where the expansion of the inflow area A_1 is hindered by the surrounding turbines. Thus, in such a system a coupling through a larger pressure system can be expected, with a pressure gradient not only in the streamwise direction, but also in the spanwise direction. An additional relation for the pressure system, may be, e.g., obtained from an atmospheric perturbation model (Allaerts and Meyers, 2019; Devesse et al., 2022; Stipa et al., 2024; Devesse et al., 2024a, b; see also the open-source model WAYVE) which incidentally also parametrize the more complex relation between capping inversion displacement and gravity wave excitation in wind farms. It is however not in the scope of the current work to develop such a coupling. Instead, we will evaluate the pressure system arising in our large-eddy simulations in more detail, and use Δp_{NW} measured from the simulations as an additional input to evaluate the system above, comparing its output in terms of power and thrust versus those obtained directly from LES.

4 Results and discussion

4.1 Velocity deficit and wake recovery

4.1.1 Induction zone and near wake analysis

Here we look in more detail into the wake development for the different simulation cases. In Fig. 4 we present the streamwise centreline velocity (U_c), scaled by the free-stream velocity at hub height (U_∞) and averaged over the turbines in each row, for all cases, providing a general overview of the differences and possible similarities in wake development. In Fig. 4a two regions of interest are depicted, i.e. the induction zone and near wake on the one hand, and the far wake on the other hand. We use the minimum of the velocity to mark the end of the near wake region, which can depend significantly on the boundary layer height H as, e.g., seen in Fig. 4a. The start of the far wake region is selected $x/D = 6$ for all cases. As we will show below (see Fig. 6a and b), the far wake velocity profile can be fitted very well with a Gaussian function, which we can use to quantify the wake recovery behaviour in detail. Upstream of our selected starting point for the far wake, such a fit does not work very well, as the wake profile is transitioning from a top-hat to a Gaussian shape, potentially requiring more advanced fitting shapes.

First looking at the near wake in Fig. 4, we observe that the maximum velocity deficit in the near wake decreases with S and H, i.e. with increasing blockage, for all cases. Consequently, we also expect the axial induction factor (a) to depend significantly on blockage. In Fig. 5 we show the axial induction factor for all cases, as obtained from the LES, as function of the inverse geometrical blockage ratio ($A/A_d = 4SH/\pi D^2$), i.e. cases with strong blockage have a low inverse geometrical blockage ratio. To this end, we evaluate $a = 1 - U_d/U_{in}$, with U_d the disk averaged (and time averaged) velocity, and U_{in} the turbine inflow velocity at hub height. For all infinite row cases, we average in addition over the different turbines in the row (since they have in principle the same induction factor); for the finite row cases, we show the induction of the individual
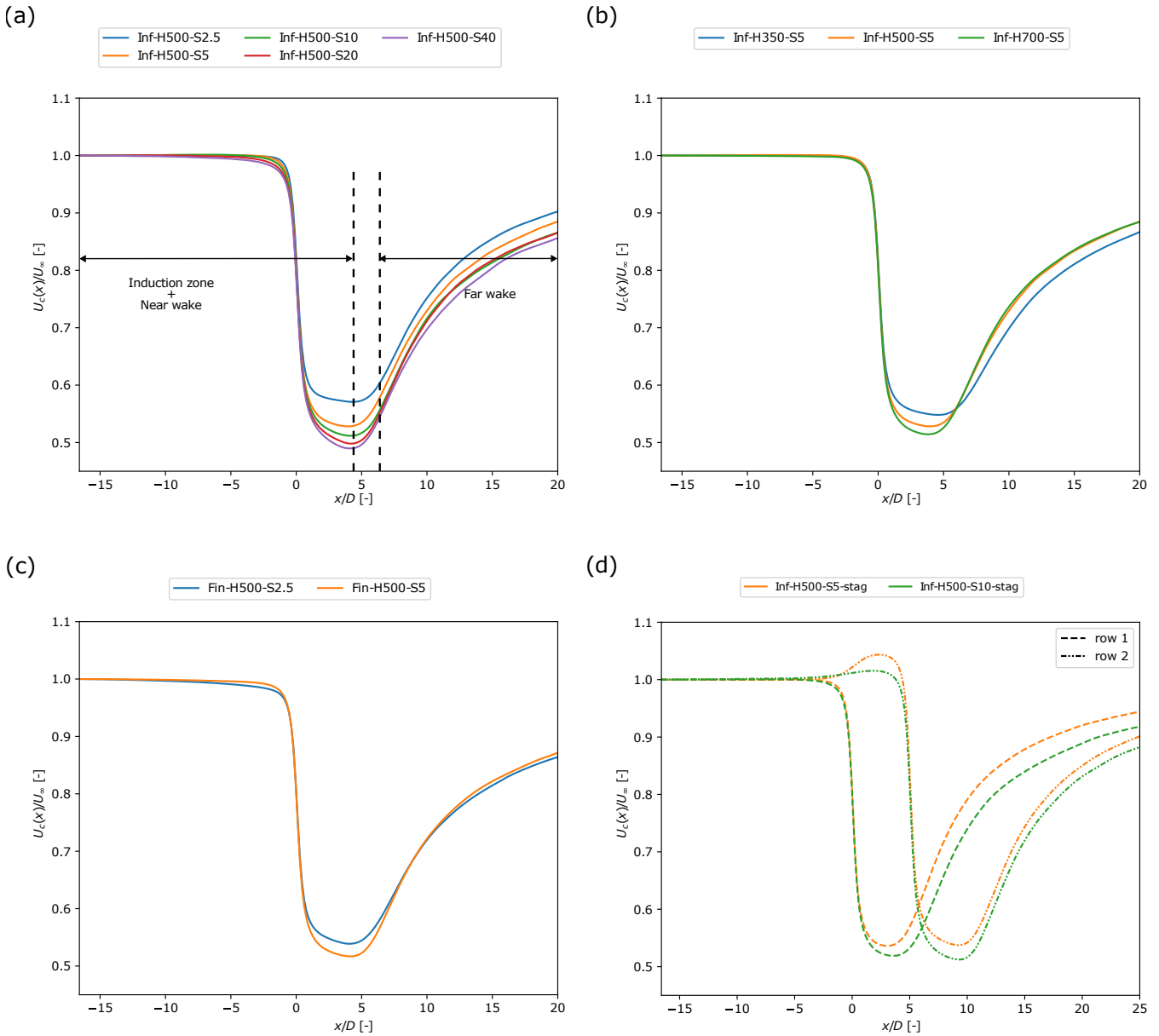
Figure 4. Streamwise centreline velocity U_c, scaled with the free stream velocity U_∞, averaged over all turbines within the row for (a) single infinite row cases with $H = 500$ m, (b) single infinite row cases with $S = 5D$, (c) finite row cases and (d) staggered infinite row cases.

turbines. For all cases, except the staggered row cases, U_{in} is simply the far upstream inflow velocity at hub height U_∞, obtained from the concurrent precursor simulation. It is calculated as the streamwise velocity averaged along the streamwise line passing through the turbine hub location. For the staggered cases, in particular the second row, we observe however a significant acceleration of the flow upstream of the second-row turbines, which passes in between the turbines of the first row

230   (see Fig. 4d). Therefore, for this row, we use the maximum velocity upstream of the turbine for U_{in}. Looking in particular at the comparison between the axial induction factor in the first and second row of the staggered row case and single infinite row case, for same boundary layer height (and thus same inverse geometrical blockage ratio $A/A_d = 4SH/\pi D^2$), we observe that they are nearly equal and within averaging uncertainty, indicating that our choice of U_{in} works well. Later (see Sect. 4) we will show that this definition also leads to good performance of the simple model (Eqs. 4–8) when compared to LES data.

235   The error bars in Fig. 5 are constructed using moving block bootstrapping (MBB). Time averaging was performed over a time interval $T_{av} = 10000$s, sampling every 2 seconds. The MBB method splits the original time series with n data samples into $N_b = n - L + 1$ overlapping blocks containing L samples. From this pool of N_b blocks, a new time series is assembled by randomly choosing $K = n/L$ blocks with replacement and then the mean of the new time series is calculated. This process is repeated B times, resulting in a distribution of means. Finally the 2.5 % and 97.5 % percentiles of the distribution of means

240   mark the 95 % confidence interval. The MBB approach is defined by selecting the number of bootstrapping runs B and the size of the blocks L. The preliminary sensitivity study showed convergence, for $L = 20$, to a robust value that does not significantly change for longer block lengths. A similar sensitivity study showed that $B = 1500$ iterations is sufficient for this purpose.

    Looking further at Fig. 5a, we observe that the axial induction factor converges to $a \approx 0.264$ for high inverse geometrical blockage ratio (A/A_d high). This is inline with the expected Betz–Joukowsky value of $a = C'_T/(4 + C'_T) = 0.265$. The plot

245   also shows, that the finite row cases have an overall higher induction than their infinite row counterparts for the same inverse geometrical blockage ratio, implying that less blockage is present in the finite row cases. This will be explained further in Sect. 4.2.2. Overall, at low inverse geometrical blockage ratios (A/A_d low), we see a significant deviation of the induction factor towards lower values than the expected Betz–Joukowsky value. This difference further translates towards the far wake as seen before in Fig. 4. It is further interesting to look at the induced near wake velocity. In Fig. 5b, we show $(1 - U_w/U_{in})/(2a)$,

250   where U_w evaluated as the minimum wake velocity (see Fig. 4) at hub height. Note that the expected Betz–Joukowsky value of this ratio corresponds to one. As can be seen in Figure 5b, the induced near wake velocity nears the Betz–Joukowsky value, for high inverse geometrical blockage, but some differences remain. In particular the onset of wake recovery can reduce the maximum wake deficit expected from the pure inviscid solution predicted by the Betz–Joukowsky. Next to that, subtle effects, related to the presence of shear may also play a role. When looking at decreasing inverse geometric blockage ratio's,

255   we observe that not only a lower induction results at the turbine disk, but an even lower wake deficit in the near wake (i.e. $(1 - U_w/U_{in}) < 2a$).

4.1.2   Far wake analysis

We first discuss the evolution of the far wake as seen in a horizontal plane at hub height. Here we observe that a classical Gaussian shape function provides good fits along the downstream direction. This is in line with Liu et al. (2002), Shamsoddin

260   and Porté-Agel (2017, 2018), who observed that the their turbulent wake profiles retained a Gaussian shape under non-zero pressure gradient conditions. Thus we use a Gaussian profile (Pope, 2000),

$$\frac{U_s(x) - u(x,y)}{U_s(x)} = C(x)e^{-y^2/(2\delta_y(x)^2)}, \tag{9}$$
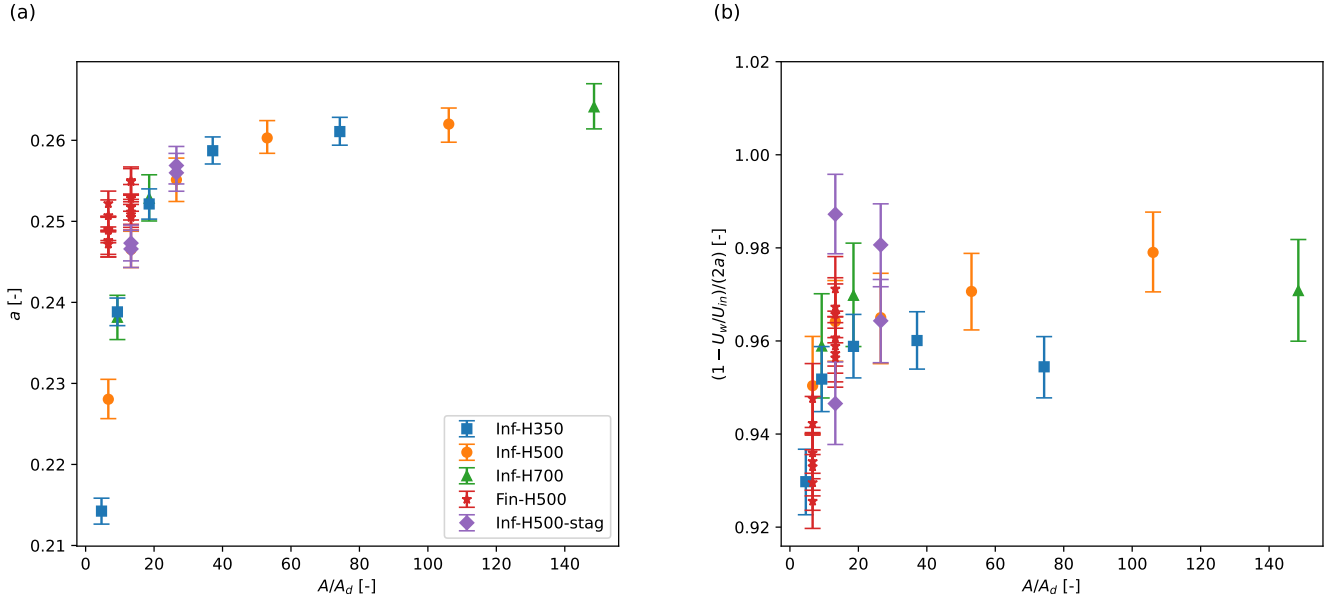
Figure 5. (a) Axial induction factor a and (b) induced near wake velocity scaled with the axial induction obtained from LES, as function of the inverse geometrical blockage ratio $A/A_d = 4SH/(\pi D^2)$. The row averages are shown for the infinite row cases, while individual turbine values are shown for the finite row cases. Error bars represent 95% confidence intervals, obtained using moving block bootstrapping.

where $U_s(x)$ is the streamwise velocity far from the wake centre, $u(x,y)$ is the wake velocity, $C(x)$ is the normalised wake velocity deficit and $\delta_y(x)$ is the horizontal wake width. We fit this function to the LES data, thus extracting $U_s(x)$, $C(x)$ and
265 $\delta_y(x)$ as a result at each downstream position. Figures 6a and b, show indeed that the horizontal wake profile, averaged across turbines in the row, has a Gaussian shape in the specified downstream range. Similar profiles are also found for all the other simulation cases.

Figures 7a-c show the evolution of $C(x)$ and (d-f) show the evolution of $\delta_y(x)$, averaged over the different turbines in each row, scaled with their values at the start of the far wake for all simulations. The downstream distance is reformulated as
270 $(x - x_0)/\delta_{y,0}$, with x_0 the starting location of the far wake. Figures 7b and e show that the far wake development of the two infinite staggered rows, as well as the single finite row, follow the same trend as the single infinite row. As H increases, $C(x)$ remains approximately the same, while $\delta_y(x)$ spreads faster. In particular, the difference between $H = 350$ m and the other two BL heights is clearly visible. This can be understood by looking at the evolution of the vertical velocity profiles (in the wake centre) shown in Fig. 8 for infinite row cases with $S = 5D$. In particular for cases H350 is observed that vertical spreading of
275 the wake is limited by the presence of the rigid-lid. Note that the turbine tip height (270 m) is not much lower than the BL height in this case. Thus for this case, the turbine far wake behaves less as an axisymmetric and more as a planar wake, which is known to have lower spreading rate (Pope, 2000).

(a)   (b)
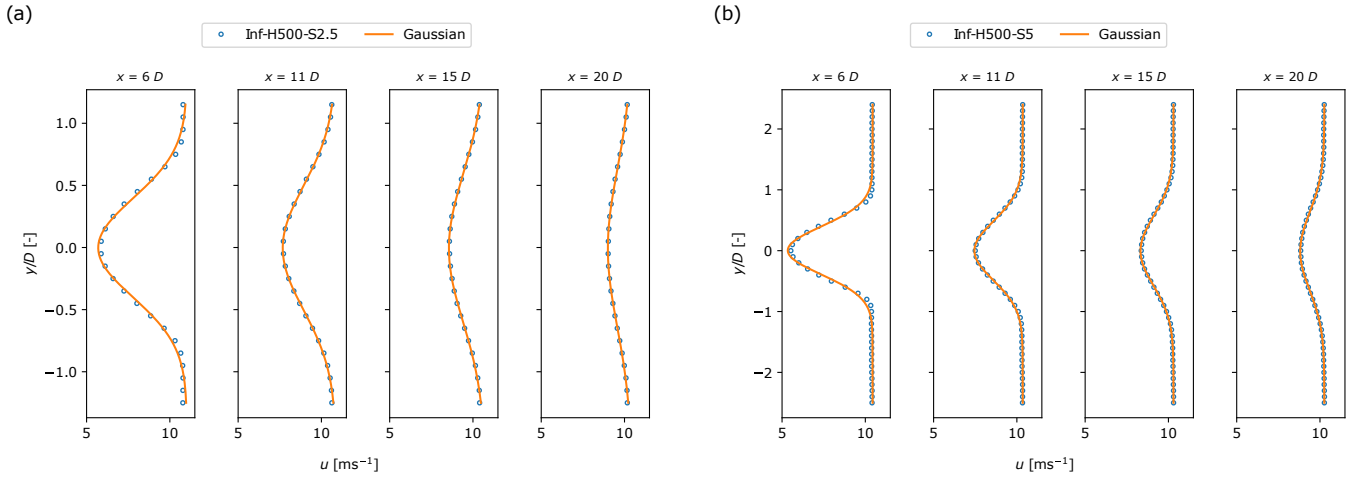
Figure 6. Horizontal wake velocity profiles, averaged over the turbines within the row, at different positions downstream in the far wake. The circles show LES results for the cases (a) Inf-H500-S2.5 and (b) Inf-H500-S5 and the orange lines represent the classical Gaussian shape function from Eq. 9.

Returning to Fig. 7, we further observe that for constant H, the $C(x)$ and $\delta_y(x)$ curves align closely across varying S values, and thus varying adverse pressure strengths. This contrasts with the findings of Liu et al. (2002); Shamsoddin and Porté-Agel (2018), which suggest that a stronger adverse pressure gradient will slow down the wake deficit recovery and enhance wake spreading. However, the adverse pressure gradient in the far wake of our simulations (normalized by ρU_{in}^2), turns out to be at least an order of magnitude smaller than the one in Liu et al. (2002) and Shamsoddin and Porté-Agel (2018), which they obtained as a result of diverging domain boundaries. Finally for cases with $S = 2.5D$, (and also $S = 5D$ for the two staggered rows) neighbouring wakes start touching at $x \approx 16D$ (see Fig. 6a). This also drastically changes the wake spreading rate, as wakes essentially start to merge.

4.2 Evaluation of near wake blockage model

We now focus on the effect of blockage on the power and thrust, and evaluate the simple near wake blockage model developed based on momentum theory (Eqs. 4–8) against the LES data. To this end, we evaluate from the large-eddy simulations

$$C_P = \frac{FU_d}{\frac{1}{2}A_d U_{in}^3} = C_T'\left(\frac{U_d}{U_{in}}\right)^3 = C_T'(1-a)^3, \tag{10}$$

$$C_T = \frac{F}{\frac{1}{2}A_d U_{in}^2} = C_t'\left(\frac{U_d}{U_{in}}\right)^2 = C_t'(1-a)^2, \tag{11}$$

where a is evaluated as discussed above (see Sect. 4.1.1 and Fig. 5).
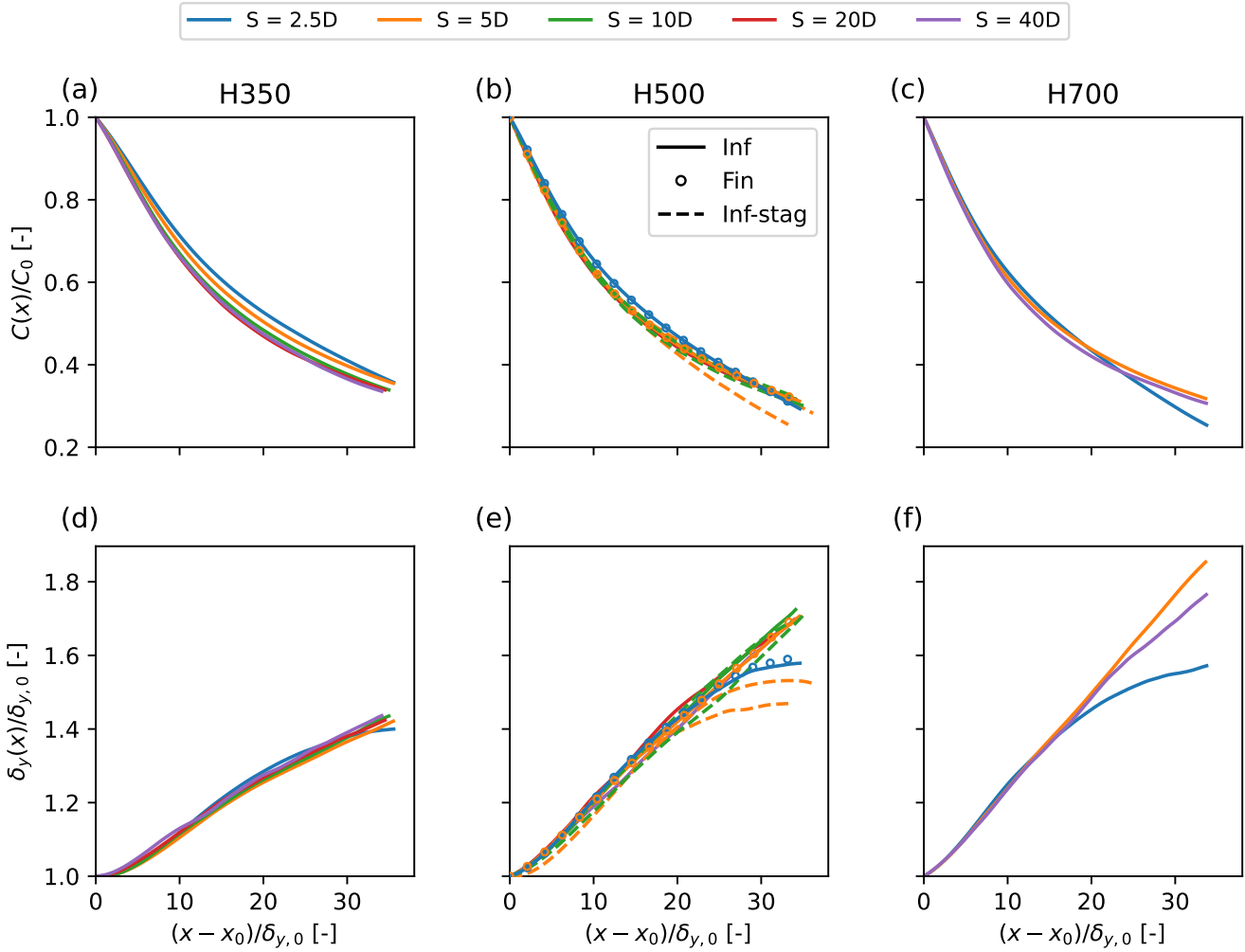
Figure 7. Evolution of the far wake properties for all simulations, averaged over the turbines within the row. (a–c) Normalised wake velocity deficit $C(x)$ and (d-f) wake width $\delta(x)$ scaled with their respective value at the start of the far wake $C_0 = C(x_0)$ and $\delta_{y,0} = \delta_{y,0}(x_0)$, for various H, plotted against the downstream distance $(x - x_0)/\delta_{y,0}$, with $x_0 = 6D$ the starting location of the far wake.

4.2.1 Infinite row

For the infinite row cases, all input variables ($A_1 = A_2 = SH, A_d, C'_t$ and U_{in}) required for the blockage model are known. U_{in} is obtained from the concurrent precursor as, the streamwise velocity averaged over the streamwise line through the turbine hub location, except in case of the second staggered row, where U_{in} is derived from the wind farm simulation, as the maximum velocity upstream of the turbine. With C'_T fixed, C_P and C_T depend on the ratio U_d/U_{in} (i.e. the induction factor), which
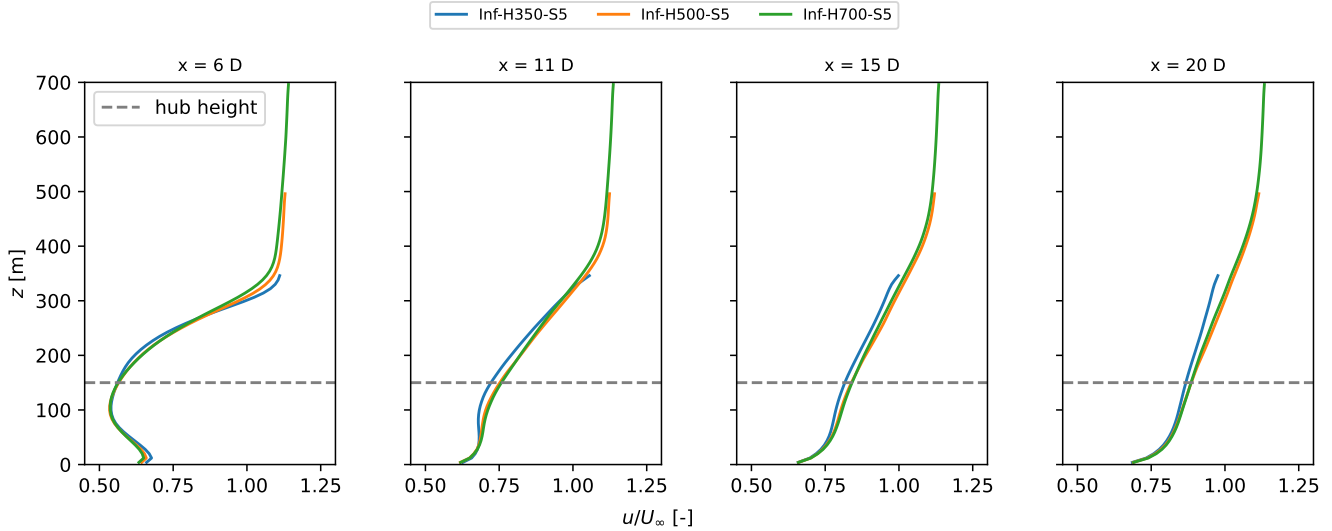
Figure 8. Vertical wake velocity profiles at different downstream positions, averaged over the turbines within the row for the infinite row turbine cases with $S = 5D$ and $H = 350, 500$ and 700 m.

depends solely on the inverse geometrical blockage ratio. Thus for varying U_{in}, but SH constant, the model returns a single C_P and C_T value

Figures 9 (a) and (c), show $\langle C_P \rangle_{row}$ and $\langle C_T \rangle_{row}$ as function of S/D, scaled with $C_{P,0}$ and $C_{T,0}$, which are the C_P and
300   C_T values of a single free standing turbine without blockage. To this end, we used the turbine in case Inf-H700-S40, since the geometric blockage ratio $A_d/A = 0.0067$, which can be regarded as negligible (Segalini and Inghels, 2014). As can be observed in the figure, the model agrees well with the LES data, although it tends to overpredict both thrust and power, in particular at high blockage ratios. We further see that at a turbine spacing of $S/D = 5$, there is a notable increase in $\langle C_P \rangle_{row}$ of 11%, 8% and 5% for $H = 350, 500$ and 700 m, compared to the single free standing turbine.

305   Finally, Fig.9b and d show $\langle C_P \rangle_{row}/C_{P,0}$ and $\langle C_T \rangle_{row}/C_{T,0}$ results from figure 9a and c, as a function of the inverse geometrical blockage ratio (A/A_d). As mentioned above, the model output in this case only depends on the blockage ratio. We observe that the different LES results also collapse well onto a single curve when this scaling is used

4.2.2 Finite row

For the finite row cases, the known input variables are: $A_1 = SH$, A_d, C_t' and U_{in} which is obtained from the concurrent
310   precursor as, the streamwise velocity averaged over the streamwise line through the turbine hub location. For this case, the area A_2 is not know a priori, nor is the favourable pressure gradient known. This would require an additional closure relation that related the wind-farm thrust to the larger pressure system around the farm.

To appraise this large scale pressure system, we evaluate for the finite row cases in Fig. 10a the pressure drop $-\Delta p_{nw}(y)$, only containing the pressure perturbations superimposed on the background pressure gradient (see Eq. 3), between the domain
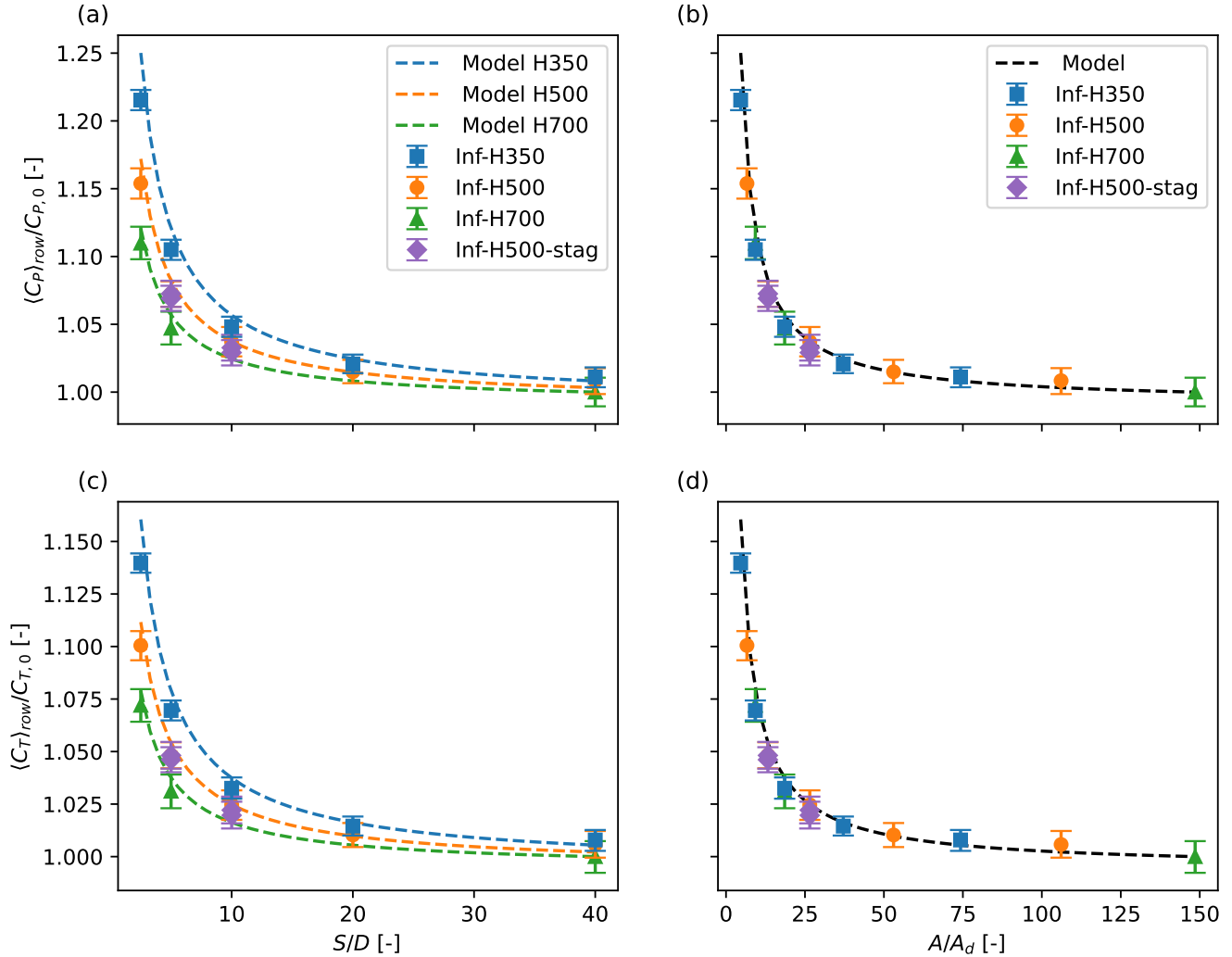
Figure 9. (a) Row averaged scaled power coefficient $\langle C_P \rangle_{row}/C_{P,0}$ as function of spacing S/D and (b) as function of inverse geometric blockage ratio A/A_d, for varying boundary layer heights H. (c) Row averaged scaled thrust coefficient $\langle C_T \rangle_{row}/C_{T,0}$ as function of S/D and (d) as function of A/A_d, for varying H. Data shown for all infinite row cases (single and staggered). $C_{P,0}$ and $C_{T,0}$ are the C_P and C_T of a single free-standing turbine with no blockage, i.e. case Inf-H700-S40. The error bars are bootstrap 95 % confidence intervals.

315 inlet and the end of the near wake ($x \approx 4D$), averaged over H, as function of the spanwise direction y, where $y = 0$ is located at the row centre. It is observed that the pressure drop reaches a maximum at the row centre, decreasing for larger absolute values of y until a (near zero) pressure difference is reached far from the turbine row. As expected, the wakes of turbines at the edge of the row have more space for lateral expansion, and thus experience a lower $|\Delta p_{NW}|$ than those at the centre, where expansion is constrained by neighbouring turbines and the boundary layer height. Looking in more detail at the pressure drop
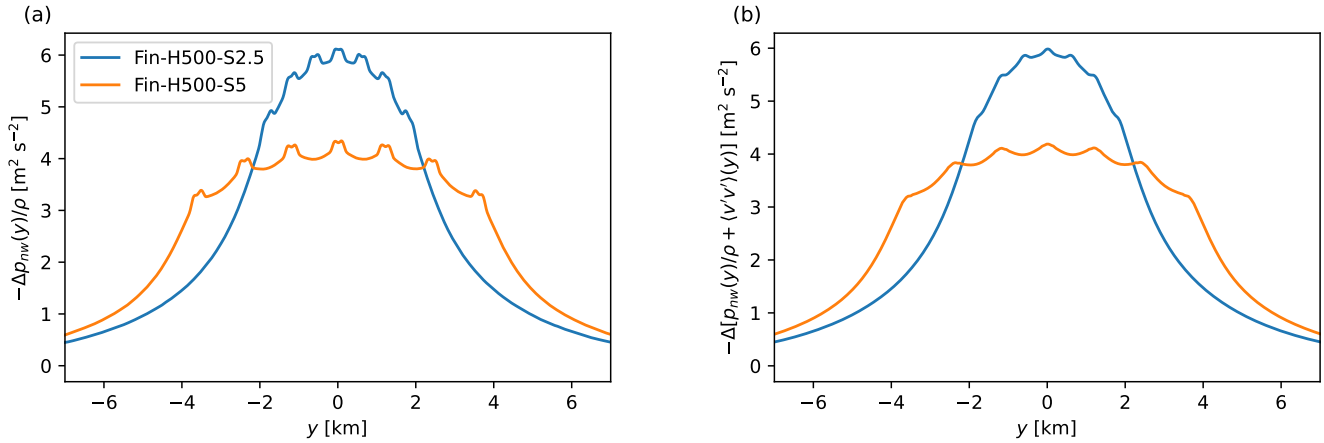
Figure 10. (a) Pressure drop at the end of the near wake ($-\Delta p_{nw}(y)$) and (b) pressure drop plus the lateral Reynold stress ($\langle v'v'(y)\rangle$), averaged over H, as function of the spanwise direction, where y = 0 km is the location of the centre turbine in the row.

320 around the turbines, we see small local variations. These are in part related to the normal Reynolds stresses. For a conventional axisymmetric wake it is well understood that $(1/\rho)\partial p/\partial r + \partial\langle u_r'u_r'\rangle/\partial r = 0$, with $\langle u_r'u_r'\rangle$ the radial normal stress (Pope, 2000). Thus, in Fig. 10b we have plotted $\Delta[p/\rho + \langle v'v'\rangle]$ as function of y (and averaged over the BL height). Note that the spanwise fluctuation v' is strictly speaking only in the radial direction in a horizontal plane, but as appreciated in the figure the local variations in the pressure drop (in particular in the wake centres) disappear.

325 To close the system of equations (4–8), we will use Δp_{NW} as observed in the LES, and compare the thrust and power output of the near wake blockage model with that of the LES. To obtain Δp_{NW}, we simply average $\Delta p_{nw}(y)$ over the interval $[y_h - S/2, y_h + S/2]$ for each turbine in the row. We note that a pressure closure at the farm level could, e.g., be provided by typical gravity wave models such as, e.g., WAYVE Allaerts and Meyers, 2019; Devesse et al., 2022; Stipa et al., 2024; Devesse et al., 2024a, b, in which a coupling between the larger atmospheric flow around the farm and local wake models is foreseen.
330 However, here we aim specifically at assessing the relevance of a simple near wake model that accounts for a favourable pressure drop. A full interaction with effects of gravity-wave feedback is a topic of future research.

Next to closing the system with the pressure gradient from LES, we also evaluate the two-scale model proposed by Nishino and Willden (2012, 2013) for half-open channel flows (formulated in the context of tidal turbines). At the turbine scale (i.e. the near wake model), they use relations similar to (4–8), while at the farm scale, they use classical Froude momentum theory
335 (without) pressure gradient to obtain a relation for the overall farm wake expansion. By further assuming that all turbines in a row produce the same power, they arrive at a closed system of equations. Although, the drawback of the approach is that there is no spanwise variation in turbine power output, it does allow for an overall assessment of farm power. We refer to Nishino and Willden (2012, 2013) for more details about this model and its implementation.

Figure 11a and b present the C_P and C_T for each turbine of cases Fin-H500-S2.5 and Fin-H500-S5, together with the
340 predicted values from the extended Froude momentum theory model and the model developed by Nishino and Willden (2012).
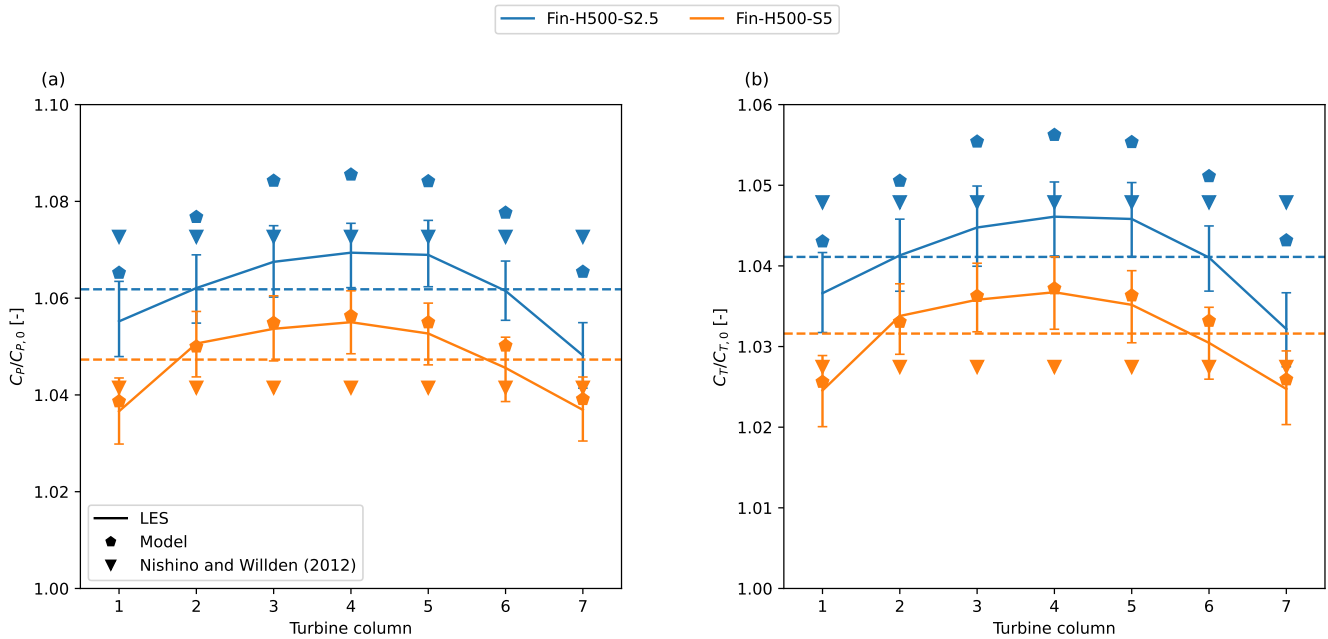
Figure 11. (a) C_P and (b) C_T for each turbine in the finite row cases, as found by the large-eddy simulations, the extended Froude momentum theory model and the model from Nishino and Willden (2012). The error bars are bootstrap 95 % confidence intervals. Horizontal dashed lines mark the row averaged values of the corresponding LES cases.

We notice that $\langle C_P \rangle_{row}$ is higher for the case with smaller S, i.e. stronger blockage, which was also observed for the infinite row cases. Additionally, the C_P value increases towards the row centre, with $C_{P,centre} > \langle C_P \rangle_{row} > C_{P,side}$, which was also found in the RANS results of Nishino and Draper (2015). The same findings are observed for the C_T data in Fig. 11b. We appreciate from the figures that for the high blockage case (S2.5) both models overpredict the power. For the lower blockage case (S5), Nishino and Willden's (2012; 2013) model is reasonably close to the row average predicted by the LES, whereas our model manages to predict also the shape of power and thrust along the row rather well.

Finally, in Fig. 12 the power and thrust coefficients C_P and C_T, are provided for all simulations, assembling the results form Figs. 9 and 11 into one figure. Overall, the model agrees well with the LES data, although it tends to overpredict both thrust and power, in particular at high blockage ratios, for both the infinite and finite row cases the error increases. We observe smaller increases in C_P and C_T for the finite row cases, compared to their infinite row counterpart, since less surrounding turbines are present to constraint the inflow from expanding, thus resulting in weaker pressure drops and blockage.

5 Conclusions

This study set out to analyse the effect of blockage on the wake development behind turbines and the turbine power. Recent research by Lanzilao and Meyers (2024) discovered a strong positive correlation between the favourable pressure gradient in the
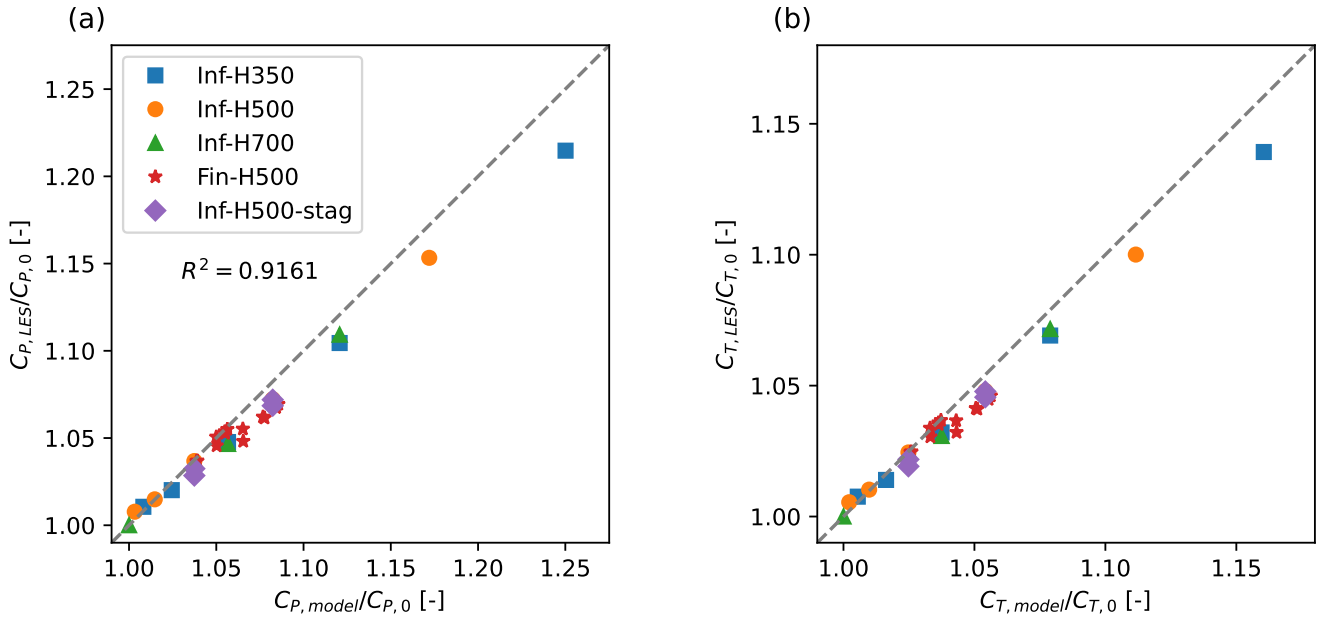
Figure 12. (a) The scaled power coefficient $C_{P,LES}/C_{P,0}$ and (b) The scaled thrust coefficient $C_{T,LES}/C_{T,0}$, as found by the extended Froude momentum theory model (x-axis) and the large-eddy simulations (y-axis). The squares, circles and triangles represent the row averaged values of the single infinite row cases, with respective H. The stars represent the values of the individual turbines for the finite row cases. The diamonds represent the row averaged values of the infinite staggered row cases. The R^2 value denotes the coefficient of determination.

355 farm and the wake efficiency η_w. This implies that the favourable pressure gradient, induced by blockage, enhances the wake recovery mechanism. We performed 17 LES simulations consisting of infinite and finite single turbine rows, as well as two staggered turbine rows, with constant C_T', in an idealised ABL setting. Blockage conditions were artificially introduced using a rigid lid, inducing a favourable pressure difference ($\Delta p_{NW} < 0$) over the turbine row and an adverse pressure difference ($\Delta p_{FW} > 0$) in the far wake. The blockage strength was adjusted by varying the turbine spacing ($S/D = 2.5, 5, 10, 20, 40$) and
360 boundary layer height ($H = 350, 500, 700$ m).

A strong positive correlation was identified between Δp_{NW} and both the power coefficient (C_P) and thrust coefficient (C_T). Specifically, as S and H decrease, $-\Delta p_{NW}$, C_P, and C_T increase. Simultaneously, the rotor disk experiences lower induction, and the near wake shows a reduced wake deficit. Specifically, the infinite row cases, at realistic spacings $S/D = 5$ already show a significant increase in C_P of 11%, 8% and 5% for $H = 350, 500$ and 700 m respectively, compared to a single free standing
365 turbine without blockage. Smaller increases are found for the finite row cases, since less surrounding turbines are present to constraint the inflow from expanding, thus resulting in weaker pressure drops and blockage. In this case, power and thrust are distributed, are maximum at the centre of the row, and also Δp_{NW} increases towards the centre of the row.

The reduction in near wake velocity deficit due to blockage also leads to smaller velocity deficits and narrower wake widths in the far wake. However, blockage has a negligible direct effect on far wake development when scaling the far wake deficit and width with their initial far wake values. We note that the adverse pressure gradient in the far wake that we observed in our study, is at least an order of magnitude smaller than those found by, (Liu et al., 2002; Shamsoddin and Porté-Agel, 2018) in diverging channels (for which case adverse effects on wake recovery were noticed). However, we do see a profound effect of H on the wake recovery, with higher boundary layers leading to faster recovery. This relates to the fact the wake can more freely expand vertically in high-boundary layer cases, into a larger region of high-speed flow than for shallow boundary layers.

We further developed an analytical model consisting of five equations to predict the blockage effect on near wake properties (similar to earlier models to correct for wind tunnel blockage in experiments – see Mikkelsen and Sørensen, 2002; Werle, 2010; Segalini and Inghels, 2014). Based on theoretical Froude momentum theory applied to a confined domain, the model uses four known input variables: rotor diameter (D), turbine spacing (S), boundary layer height (H), disk based thrust coefficient (C_T') and inflow velocity (U_{in}), but requires one additional closure relation. In the infinite row case, this is given by $A_1 = A_2$ (no expansion possible at farm level), whereas in the finite row case, the near wake pressure drop needs to be provided. To this end, we provided the pressure drop as measured in the large-eddy simulations. Overall, we found a good agreement between LES power and thrust predictions and the simple model based on momentum theory, indicating that the latter is a suitable candidate to improve turbine power prediction under blocking conditions. In a practical implementation, such a model needs to be coupled to a farm-scale model that provides input on the large pressure distribution in the farm. Atmospheric perturbation models (Allaerts and Meyers, 2019; Devesse et al., 2022; Stipa et al., 2024; Devesse et al., 2024b; see also the open-source model WAYVE) that explicitly model the pressure feedback coming from gravity waves, are an interesting application for this. This is an ongoing topic of further research.

Author contributions. ON and JM jointly defined the methodology and set up the simulation studies in the current work. ON, JM and AP jointly developed the analytical models. ON carried out the simulations and post-processing. ON and JM wrote the manuscript.

Competing interests. At least one of the (co-)authors is a member of the editorial board of Wind Energy Science. The authors have no other competing interests to declare.

Acknowledgements. The computational resources and services used in this work were provided by the VSC (Flemish Supercomputer Center), funded by the Research Foundation - Flanders (FWO) and the Flemish Government. Additionally, the authors express their gratitude to the anonymous reviewers for their insightful comments and relevant observations on this work.

395 *Financial support.* Project Cloud4Wake, funded by Vlaamse Agentschap Innoveren & Ondernemen (VLAIO) under Blue Cluster cSBO programme (Contract number HBC.2022.0549)

References

Allaerts, D. and Meyers, J.: Boundary-layer development and gravity waves in conventionally neutral wind farms, Journal of Fluid Mechanics, 814, 95–130, https://doi.org/10.1017/jfm.2017.11, 2017.

Allaerts, D. and Meyers, J.: Gravity Waves and Wind-Farm Efficiency in Neutral and Stable Conditions, Boundary-Layer Meteorol., 166, 269–299, 2018.

Allaerts, D. and Meyers, J.: Sensitivity and feedback of wind-farm-induced gravity waves, Journal of Fluid Mechanics, 862, 990–1028, https://doi.org/10.1017/jfm.2018.969, 2019.

Bleeg, J. and Montavon, C.: Blockage effects in a single row of wind turbines, Journal of Physics: Conference Series, 2265, 022 001, https://doi.org/10.1088/1742-6596/2265/2/022001, 2022.

Bleeg, J., Purcell, M., Ruisi, R., and Traiger, E.: Wind Farm Blockage and the Consequences of Neglecting Its Impact on Energy Production, Energies, 11, https://doi.org/10.3390/en11061609, 2018.

Calaf, M., Meneveau, C., and Meyers, J.: Large eddy simulation study of fully developed wind-turbine array boundary layers, Physics of Fluids, 22, 015 110, https://doi.org/10.1063/1.3291077, 2010.

Dar, A. S. and Porté-Agel, F.: Wind turbine wakes on escarpments: A wind-tunnel study, Renewable Energy, 181, 1258–1275, https://doi.org/https://doi.org/10.1016/j.renene.2021.09.102, 2022.

Devesse, K., Lanzilao, L., Jamaer, S., van Lipzig, N., and Meyers, J.: Including realistic upper atmospheres in a wind-farm gravity-wave model, Wind Energy Science, 7, 1367–1382, https://doi.org/10.5194/wes-7-1367-2022, 2022.

Devesse, K., Lanzilao, L., and Meyers, J.: A meso–micro atmospheric perturbation model for wind farm blockage, Journal of Fluid Mechanics, 998, A63, https://doi.org/10.1017/jfm.2024.868, 2024a.

Devesse, K., Stipa, S., Brinkerhoff, J., Allaerts, D., and Meyers, J.: Comparing methods for coupling wake models to an atmospheric perturbation model in WAYVE, Journal of Physics: Conference Series, 2767, 092 079, https://doi.org/10.1088/1742-6596/2767/9/092079, 2024b.

Froude, R. E.: On the part played in propulsion by difference of fluid pressure, Transactions of the Royal Institution of Naval Architects, 30, 390–405, 1889.

Gaertner, E., Rinker, J., Sethuraman, L., Zahle, F., Anderson, B., Barter, G. E., Abbas, N. J., Meng, F., Bortolotti, P., Skrzypinski, W., Scott, G. N., Feil, R., Bredmose, H., Dykes, K., Shields, M., Allen, C., and Viselli, A.: IEA Wind TCP Task 37: Definition of the IEA 15-Megawatt Offshore Reference Wind Turbine, https://doi.org/10.2172/1603478, technical Report, United States, March 2020, 2020.

Garrett, C. and Cummins, P.: The efficiency of a turbine in a tidal channel, Journal of Fluid Mechanics, 588, 243–251, https://doi.org/10.1017/S0022112007007781, 2007.

Goit, J. and Meyers, J.: Optimal control of energy extraction in wind-farm boundary layers, Journal of Fluid Mechanics, 768, 5–50, https://doi.org/10.1017/jfm.2015.70, 2015.

Kirby, A., Dunstan, T. D., and Nishino, T.: An analytical model of momentum availability for predicting large wind farm power, Journal of Fluid Mechanics, 976, A24, https://doi.org/10.1017/jfm.2023.844, 2023.

Lanzilao, L. and Meyers, J.: Effects of self-induced gravity waves on finite wind-farm operations using a large-eddy simulation framework, Journal of Physics: Conference Series, 2265, 022 043, https://doi.org/10.1088/1742-6596/2265/2/022043, 2022.

Lanzilao, L. and Meyers, J.: A parametric large-eddy simulation study of wind-farm blockage and gravity waves in conventionally neutral boundary layers, Journal of Fluid Mechanics, 979, A54, https://doi.org/10.1017/jfm.2023.1088, 2024.

Lignarolo, L. E., Mehta, D., Stevens, R. J., Yilmaz, A. E., van Kuik, G., Andersen, S. J., Meneveau, C., Ferreira, C. J., Ragni, D., Meyers, J.,
van Bussel, G. J., and Holierhoek, J.: Validation of four LES and a vortex model against stereo-PIV measurements in the near wake of an
actuator disc and a wind turbine, Renewable Energy, 94, 510–523, 2016.

Liu, X., Thomas, F. O., and Nelson, R. C.: An experimental investigation of the planar turbulent wake in constant pressure gradient, Physics
of Fluids, 14, 2817–2838, https://doi.org/10.1063/1.1490349, 2002.

Maas, O.: Large-eddy simulation of a 15 GW wind farm: Flow effects, energy budgets and comparison with wake models, Frontiers in
Mechanical Engineering, 9, https://doi.org/10.3389/fmech.2023.1108180, 2023.

Martínez-Tossas, L. A., Churchfield, M. J., Yilmaz, A. E., Sarlak, H., Johnson, P. L., Sørensen, J. N., Meyers, J., and Meneveau, C.: Com-
parison of four large-eddy simulation research codes and effects of model coefficient and inflow turbulence in actuator-line-based wind
turbine modeling, Journal of Renewable and Sustainable Energy, 10, 033 301, 2018.

Mason, P. J. and Thomson, D. J.: Stochastic backscatter in large-eddy simulations of boundary layers, Journal of Fluid Mechanics, 242,
51–78, https://doi.org/10.1017/S0022112092002271, 1992.

McTavish, S., Feszty, D., and Nitzsche, F.: A study of the performance benefits of closely-spaced lateral wind farm configurations, Renewable
Energy, 59, 128–135, https://doi.org/https://doi.org/10.1016/j.renene.2013.03.032, 2013.

McTavish, S., Rodrigue, S., Feszty, D., and Nitzsche, F.: An investigation of in-field blockage effects in closely spaced lateral wind farm
configurations, Wind Energy, 18, 1989–2011, https://doi.org/https://doi.org/10.1002/we.1806, 2015.

Meyers, J.: Error-Landscape Assessment of Large-Eddy Simulations: A Review of the Methodology, Journal of Scientific Computing, 49,
65 – 77, 2011.

Mikkelsen, R. and Sørensen, J.: Modelling of Wind Tunnel Blocage, in: 15th IEA Symposium on the Aerodynamics of Wind Turbines,
FOI Swedish Defence Research Agency, 15th IEA Symposium on the Aerodynamics of Wind Turbines ; Conference date: 26-11-2001
Through 27-11-2001, 2002.

Munters, W., Meneveau, C., and Meyers, J.: Shifted periodic boundary conditions for simulations of wall-bounded turbulent flows, Physics
of Fluids, 28, 025 112, https://doi.org/10.1063/1.4941912, 2016.

Nishino, T. and Draper, S.: Local blockage effect for wind turbines, Journal of Physics: Conference Series, 625, 012 010,
https://doi.org/10.1088/1742-6596/625/1/012010, 2015.

Nishino, T. and Willden, R.: The efficiency of an array of tidal turbines partially blocking a wide channel, Journal of Fluid Mechanics, 708,
596–606, https://doi.org/10.1017/jfm.2012.349, 2012.

Nishino, T. and Willden, R.: Two-scale dynamics of flow past a partial cross-stream array of tidal turbines, Journal of Fluid Mechanics, 730,
https://doi.org/10.1017/jfm.2013.340, 2013.

Pope, S. B.: Turbulent Flows, Cambridge University Press, 2000.

Rankine, W. J. M.: On the mechanical principles of the action of propellers, Transactions of the Institution of Naval Architects, 6, 13, 1865.

Sanchez Gomez, M., Lundquist, J., Mirocha, J., and Arthur, R.: Investigating the Physical Mechanisms that Modify Wind Plant Blockage in
Stable Boundary Layers, Wind Energy Science, 8, 1049–1069, https://doi.org/10.5194/wes-8-1049-2023, 2023.

Segalini, A. and Dahlberg, J.-A.: Blockage effects in wind farms, Wind Energy, 23, 120–128, https://doi.org/https://doi.org/10.1002/we.2413,
2020.

Segalini, A. and Inghels, P.: Confinement effects in wind-turbine and propeller measurements, Journal of Fluid Mechanics, 756, 110–129,
https://doi.org/10.1017/jfm.2014.440, 2014.

Shamsoddin, S. and Porté-Agel, F.: Turbulent planar wakes under pressure gradient conditions, Journal of Fluid Mechanics, 830, R4, https://doi.org/10.1017/jfm.2017.649, 2017.

Shamsoddin, S. and Porté-Agel, F.: A model for the effect of pressure gradient on turbulent axisymmetric wakes, Journal of Fluid Mechanics, 837, R3, https://doi.org/10.1017/jfm.2017.864, 2018.

475 Shapiro, C. R., Gayme, D. F., and Meneveau, C.: Filtered actuator disks: Theory and application to wind turbine models in large eddy simulation, Wind Energy, 22, 1414–1420, https://doi.org/https://doi.org/10.1002/we.2376, 2019.

Smith, R. B.: The wind farm pressure field, Wind Energy Science, 9, 253–261, https://doi.org/10.5194/wes-9-253-2024, 2024.

Sood, I., Simon, E., Vitsas, A., Blockmans, B., Larsen, G. C., and Meyers, J.: Comparison of large eddy simulations against measurements from the Lillgrund offshore wind farm, Wind Energy Science, 7, 2469–2489, https://doi.org/10.5194/wes-7-2469-2022, 2022.

480 Stevens, R. J., Graham, J., and Meneveau, C.: A concurrent precursor inflow method for Large Eddy Simulations and applications to finite length wind farms, Renewable Energy, 68, 46–50, https://doi.org/https://doi.org/10.1016/j.renene.2014.01.024, 2014.

Stipa, S., Ajay, A., Allaerts, D., and Brinkerhoff, J.: The multi-scale coupled model: a new framework capturing wind farm–atmosphere interaction and global blockage effects, Wind Energy Science, 9, 1123–1152, https://doi.org/10.5194/wes-9-1123-2024, 2024.

Strickland, J. and Stevens, R.: Effect of thrust coefficient on the flow blockage effects in closely-spaced spanwise-infinite turbine arrays,
485 Journal of Physics: Conference Series, 1618, 062 069, https://doi.org/10.1088/1742-6596/1618/6/062069, 2020.

Strickland, J. M. and Stevens, R. J.: Investigating wind farm blockage in a neutral boundary layer using large-eddy simulations, European Journal of Mechanics - B/Fluids, 95, 303–314, https://doi.org/https://doi.org/10.1016/j.euromechflu.2022.05.004, 2022.

Taylor, P. K. and Yelland, M. J.: The Dependence of Sea Surface Roughness on the Height and Steepness of the Waves, Journal of Physical Oceanography, 31, 572 – 590, https://doi.org/10.1175/1520-0485(2001)031<0572:TDOSSR>2.0.CO;2, 2001.

490 Verstappen, R. and Veldman, A.: Symmetry-preserving discretization of turbulent flow, Journal of Computational Physics, 187, 343–368, https://doi.org/10.1016/S0021-9991(03)00126-8, 2003.

Werle, M. J.: Wind Turbine Wall-Blockage Performance Corrections, Journal of Propulsion and Power, 26, 1317–1321, https://doi.org/10.2514/1.44602, 2010.

Wu, K. L. and Porté-Agel, F.: Flow Adjustment Inside and Around Large Finite-Size Wind Farms, Energies, 10,
495 https://doi.org/10.3390/en10122164, 2017.